Stability Analysis of Active Front End and Permanent Magnet Synchronous Generator With Back EMF-Based Sensorless Control for DC Marine Vessels

Young-Wook Kim, *Graduate Student Member, IEEE*, and Seung-Ki Sul, *Fellow, IEEE*

***Abstract*—This article studies the influence of sensorless control on the permanent magnet synchronous generator (PMSG) and pulsewidth modulation (PWM) converter (active front end rectifier, AFE) system for dc marine vessels. Back EMF-based sensorless control is adopted in this article because the minimum speed of PMSG in a dc marine vessel is enough for obtaining a sufficient back EMF signal. First, the output impedance of "PMSG+AFE" system with a typical topology and controller is deduced by small-signal analysis. The stability analysis with constant power load (CPL) is analyzed, including the influence of sensorless control bandwidth on PMSG with a significant per-unit impedance value. Since the inductance parameter affects both the current control and sensorless control, the influence of error in the estimated inductance parameter on the stability of "PMSG+AFE" system is analyzed. To verify the proposed impedance model, output impedance is measured in the simulation and experiment. The stability analysis with the proposed impedance model and load impedance of CPL is provided in MATLAB, and simulation results and experimental measurements are given to verify the analysis.**

***Index Terms*—Active front end (AFE), dc impedance, EMF-based sensorless control, permanent magnet synchronous generator (PMSG), small-signal model, stability analysis.**

I. Introduction

DC grid system has been applied to marine vessels for their advantages, such as high efficiency, high reliability, and simple controllability [1], [2]. In the ac grid system, since the frequency must be constant, the engine should run at a constant speed. However, in the dc grid system, the dc voltage does not have a frequency, and variable speed operation of the prime mover is possible with the smallest fuel consumption depending on the load.

Manuscript received 18 July 2022; revised 23 October 2022; accepted 26 December 2022. Date of publication 3 January 2023; date of current version 14 February 2023. This work was supported by the BK21 FOUR (Fostering Outstanding Universities for Research), funded by the Ministry of Education (MOE, Korea) and National Research Foundation of Korea (NRF). Recommended for publication by Associate Editor D. Zhang. *(Corresponding author: Seung-Ki Sul.)*

The authors are with the Department of Electrical and Computer Engineering, Seoul National University, Seoul 08826, South Korea (e-mail: dandan2@snu.ac.kr; sulsk@snu.ac.kr).

Color versions of one or more figures in this article are available at https://doi.org/10.1109/TPEL.2022.3233889.

Digital Object Identifier 10.1109/TPEL.2022.3233889

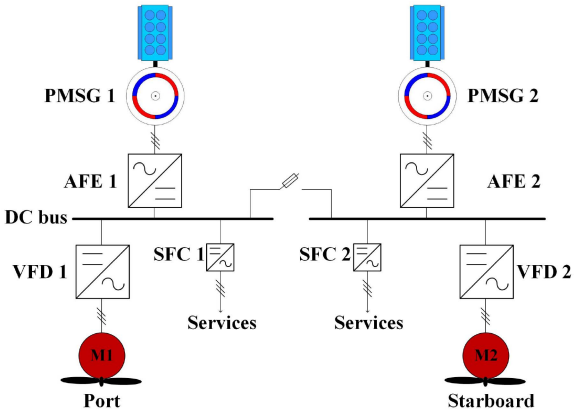

Fig. 1. Typical structure of dc grid system for electric propulsion ship.

The generation part of the dc grid system consists of a generator and a rectifier. In general, a wound rotor synchronous generator and diode rectifier (diode front end) has been widely applied [3], [4]. However, in recent years, permanent magnet synchronous generator (PMSG) and pulsewidth modulation (PWM) converter (active front end, AFE) have been applied for their higher efficiency [5], [6]. Fig. 1 shows a typical structure of a dc grid system for an electric propulsion vessel [7], [8]. The load consists of a variable frequency drive (VFD) for the propulsion motor and a static frequency converter (SFC) for the service load in the vessel.

The AFE and the VFD are the same power electronic converters in controlling rotating electric machines, except for internal control. The AFE receives ac voltage from the generator as an input to control dc voltage, whereas the VFD receives stable dc voltage as an input to control the motor's torque. In the existing ac electric propulsion system, the VFD often already includes the AFE at the input stage as a rectifier. Therefore, many companies already provide electric propulsion systems with AFE-related technology [9], [10] as a front end. The "PMSG+AFE" system and "propulsion motor+VFD" system require a position sensor: encoder, resolver, hall sensor, etc. Generally, these electromechanical rotor position sensors lead to undesirable effects on the system: additional cost and volume, noise, and reliability

issues. Especially for the electric propulsion vessels, there are difficulties in ship design because of the increased axial length due to the position sensor. In addition, the position sensor is pointed out as a weakness in system reliability and maintenance. Due to the disadvantages of the position sensor as described above, sensorless control has already been applied to the industry [9], [11].

The sensorless control methods of ac machine drives can be generally classified into two kinds according to the principle of the rotor position estimation, namely, back EMF-based method and the signal injection method [12]. Back EMF-based sensorless method extracts the rotor position information from the back EMF. It uses the electric model of the ac machine in the estimated rotor reference frame. It presents a good performance in the medium and higher speed operating region of ac machines, and many companies have commercialized it. At a standstill or very low rotating speed, the voltage signal from the back EMF is too weak to be used as the position information, and a signal can be injected to get the rotor position information. This method has also been commercialized. In marine applications, the minimum speed of the genset is set from the mechanical limitation, such as the engine's idle speed, and the oil pump's size for the lubrication. And, the minimum speed for commercial genset is approximately 50%–70% of the rated speed. Therefore, the back EMF-based sensorless method could be an appropriate option for the sensorless control of dc marine vessels.

The AFE is the power electronic converter, and interactions among the converter's control loops could result in instability at a specific operating condition. The VFD and SFC are also power electronic converters, keeping ac output voltage and frequency regardless of the dc voltage fluctuation. This behavior is called constant power load (CPL) and could destabilize the whole dc grid [13]. When the position sensorless control is applied to the AFE, the voltage source characteristics of the AFE are weakened, and thus the system stability may be endangered. However, when sensorless control is applied to the VFD, the ideal CPL characteristics of the VFD are weakened, and thus the stability of the system would be better. Therefore, the importance of analysis on the sensorless control is more critical for the AFE than for the VFD. This article analyzes the stability of the position sensorless control applied "PMSG+AFE" system.

To analyze the stability, the most applicable method is the impedance analysis which utilizes the interaction between the impedance of the source and the load. The minor loop gain is defined as the source impedance ratio to the load impedance. Under the assumption that each subsystem is stable, the stability of the whole system can be determined by the Nyquist Criterion [14], [15].

The research related to the AFE also has been applied to various types of microgrids recently, and stability analysis using dc impedance is being studied. Xue et al. [16] proposed the dc impedance of the three-phase grid-tied inverter in the *d-q* frame, considering the effect of PLL, current control, power flow control, dc voltage control, and droop control. Nian et al. [17] suggested a dc impedance reshaping method considering grid impedance and PLL. In the dc microgrid system, the AFE measures ac voltage with the sine filter and controls ac and dc voltage by detecting the phase angle of ac voltage through voltage sensing. In the case of the marine application, the AFE is directly connected to the PMSG without an ac filter, as shown in Fig. 2, and the ac and dc voltage are controlled by detecting the rotor position through the position sensor. Huang et al. [18] and Yang et al. [19] reported the dc impedance model of "PMSG+AFE" system for more electric aircraft considering the bandwidth of current control and dc voltage control. Lang et al. [20] also proposed the dc impedance model considering load distribution in parallel operation of the "PMSG+AFE" system. These models predicted the inverter impedance for feedback control where the effect of rotor position sensing was ignored. However, as far as authors are concerned, the mathematical relationship between dc impedance and sensorless control has not been quantitively analyzed. Therefore, this article proposes a full analytical model for the dc impedance of "PMSG+AFE" system in the *d-q* frame, considering the effect of sensorless control and dual-loop controls, namely current loop and voltage loop, as shown in Fig. 2.

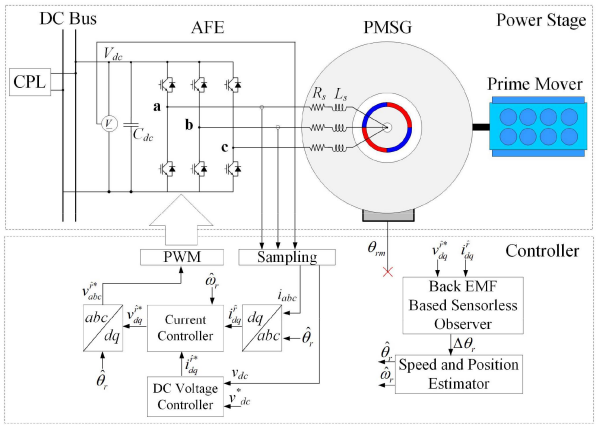

Fig. 2. "PMSG+AFE" system with dual-loop control and back EMF-based sensorless control.

The rest of this article is organized as follows. Section II models the small-signal dc impedance of the "PMSG+AFE" system considering back EMF-based sensorless control. Section III describes the stability analysis according to the dual-loop control and the parameter variation. Section IV shows the simulation and experimental results of the proposed model. Finally, Section V concludes this article.

II. Impedance Modeling of "PMSG+AFE" System

A. Power Stage and Dual-Loop Control

The voltage equation based on the rotor reference *d-q* frame for the ac side is given as

$$\begin{bmatrix} v_d^r \\ v_q^r \end{bmatrix} = \frac{v_{\rm dc}}{2} \begin{bmatrix} d_d^r \\ d_q^r \end{bmatrix} = \begin{bmatrix} R_s & -\omega_r L_{qs} \\ \omega_r L_{ds} & R_s \end{bmatrix} \begin{bmatrix} i_d^r \\ i_q^r \end{bmatrix} + \begin{bmatrix} L_{ds} \frac{d}{dt} i_d^r \\ L_{qs} \frac{d}{dt} i_q^r \end{bmatrix} + \begin{bmatrix} 0 \\ \omega_r \lambda_f \end{bmatrix} \tag{1}$$

where v_d^r and v_q^r are the output voltage, d_d^r and d_q^r are the duty factor, $v_{\rm dc}$ is dc-link voltage, i_d^r and i_q^r are measured current, R_s is the stator resistance, ω_r is the fundamental electrical angular frequency of the PMSG, λ_f is the flux linkage of the permanent magnet, and L_{ds} and L_{qs} are d-q axis stator inductance of PMSG, respectively. The superscript "r" in each variable means that the variable is presented in the rotor reference d-q frame. The rotational speed of the genset in the dc grid system depends on the load. The load slew rate of a typical MW-scale genset for the vessel is limited to 0.02 p.u./s or less [21]. Therefore, assuming that there is no perturbation in ω_r and the small-signal model for voltage and current on (1) can be derived as

$$\frac{V_{\rm dc}}{2}\begin{bmatrix}\tilde{d}_d^r\\ \tilde{d}_q^r\end{bmatrix}+\frac{\tilde{v}_{\rm dc}}{2}\begin{bmatrix}D_d^r\\ D_q^r\end{bmatrix} =\begin{bmatrix}R_s & -\Omega_r L_{qs}\\ \Omega_r L_{ds} & R_s\end{bmatrix}\begin{bmatrix}\tilde{i}_d^r\\ \tilde{i}_q^r\end{bmatrix}+\begin{bmatrix}L_{ds}\frac{d}{dt}\tilde{i}_d^r\\ L_{qs}\frac{d}{dt}\tilde{i}_q^r\end{bmatrix}. \quad (2)$$

The symbolic "$\sim$" denotes the small-signal perturbation of a variable. Capital letters of variables, e.g., $V_{\rm dc}$, D_d^r, D_q^r, I_d^r, I_q^r and Ω_r, denote the values of the dc link voltage, duty factor of AFE, current of AFE, and electrical angular speed in steady-state, respectively. Equation (2) could be converted to

$$\begin{bmatrix}\tilde{i}_d^r\\ \tilde{i}_q^r\end{bmatrix}=\begin{bmatrix}sL_{ds}+R_s & -\Omega_r L_{qs}\\ \Omega_r L_{ds} & sL_{qs}+R_s\end{bmatrix}^{-1} \times\left\{\frac{V_{dc}}{2}\begin{bmatrix}\tilde{d}_d^r\\ \tilde{d}_q^r\end{bmatrix}+\frac{1}{2}\begin{bmatrix}D_d^r\\ D_q^r\end{bmatrix}\tilde{v}_{\rm dc}\right\}$$

$$\tilde{\boldsymbol{i}}_{\boldsymbol{dq}}^{\boldsymbol{r}}=\boldsymbol{Y}_{\rm out}\tilde{\boldsymbol{d}}_{\boldsymbol{dq}}^{\boldsymbol{r}}+\boldsymbol{Y}_{\rm dc\boldsymbol{i}}\tilde{v}_{\rm dc} \quad (3)$$

in Laplace domain. $\boldsymbol{Y}_{\mathbf{out}}$ is an open loop output admittance, and $\boldsymbol{Y}_{\mathbf{dc}\boldsymbol{i}}$ is the transfer function that relates the small-signal perturbation of the dc-link voltage to the output currents in the rotor reference d-q frame. For the dc side, the energy balance in the dc-link capacitor is expressed as

$$\frac{1}{2}C_{\rm dc}v_{\rm dc}^2=E_{\rm cap}=E_{\rm in}-E_{\rm out} \quad (4)$$

where $C_{\rm dc}$ is total dc-link capacitance, $i_{\rm dc}$ is dc, $E_{\rm cap}$ is stored energy in whole dc-link capacitors, respectively.

From (4), the active power balance can be described as

$$\frac{1}{2}C_{\rm dc}\frac{dv_{\rm dc}^2}{dt}=P_{\rm in}-P_{\rm out}=v_{\rm dc}i_{\rm dc}-\frac{3}{2}(v_d^r i_d^r+v_q^r i_q^r). \quad (5)$$

$v_{\rm dc}^2$ in (5) is approximated as follows:

$$v_{\rm dc}^2=(V_{\rm dc}+\tilde{v}_{\rm dc})^2\approx V_{\rm dc}^2+2V_{\rm dc}\tilde{v}_{\rm dc}. \quad (6)$$

Substituting (6) into (5) gives a small-signal model of (5) as follows:

$$\tilde{v}_{\rm dc}=\frac{1}{sC_{\rm dc}}\tilde{i}_{\rm dc}-\frac{3}{s\cdot 4C_{\rm dc}}\left\{\begin{bmatrix}I_d^r & I_q^r\end{bmatrix}\begin{bmatrix}\tilde{d}_d^r\\ \tilde{d}_q^r\end{bmatrix}-\begin{bmatrix}D_d^r & D_q^r\end{bmatrix}\begin{bmatrix}\tilde{i}_d^r\\ \tilde{i}_q^r\end{bmatrix}\right\}$$

$$=\frac{1}{sC_{\rm dc}}\tilde{i}_{\rm dc}-\boldsymbol{G}_{\boldsymbol{d}\rm dc}\tilde{\boldsymbol{d}}_{\boldsymbol{dq}}^{\boldsymbol{r}}-\boldsymbol{G}_{\boldsymbol{i}\rm dc}\tilde{\boldsymbol{i}}_{\boldsymbol{dq}}^{\boldsymbol{r}}. \quad (7)$$

$\boldsymbol{G}_{\boldsymbol{d}\mathbf{dc}}$ links the duty factor to dc-link voltage, and $\boldsymbol{G}_{\boldsymbol{i}\mathbf{dc}}$ links output currents to dc-link voltage [22].

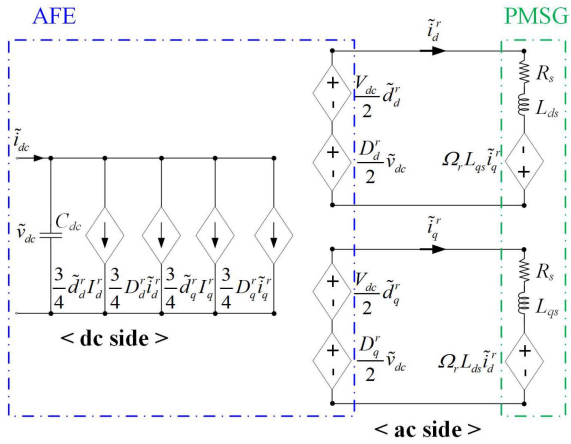

Fig. 3. Small-signal equivalent circuit of "PMSG+AFE" in d-q frame.

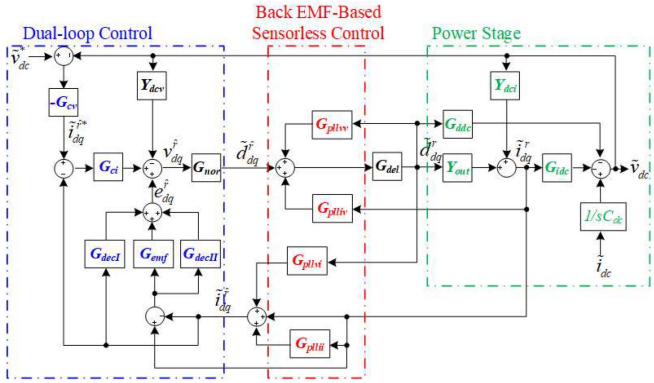

Fig. 4. Small-signal block diagram of "PMSG+AFE" system with dual-loop control and sensorless control in d-q frame.

Fig. 3 shows the small-signal equivalent circuit of the "PMSG+AFE" system. To illustrate the influence of back EMF-based sensorless control on the AFE, two d-q frames are defined, i.e., rotor reference d-q frame and estimated d-q frame [22]. And, in the steady state, (8) can be deduced from (1)

$$\frac{V_{\rm dc}}{2}\begin{bmatrix}D_d^r\\ D_q^r\end{bmatrix}=\begin{bmatrix}R_s & -\Omega_r L_{qs}\\ \Omega_r L_{ds} & R_s\end{bmatrix}\begin{bmatrix}I_d^r\\ I_q^r\end{bmatrix}+\begin{bmatrix}0\\ \Omega_r\lambda_f\end{bmatrix}. \quad (8)$$

Fig. 4 shows the small-signal block diagram of the "PMSG+AFE" system with dual-loop control and back EMF-based sensorless control in the d-q frame. It consists of three parts "dual-loop control," "back EMF-based sensorless control," and "power stage."

$\boldsymbol{G}_{\mathbf{del}}$ is in front of the "power stage" part, and it is given as

$$\boldsymbol{G}_{\rm del}=\begin{bmatrix}\frac{1-0.5T_d s}{1+0.5T_d s} & 0\\ 0 & \frac{1-0.5T_d s}{1+0.5T_d s}\end{bmatrix} \quad (9)$$

where T_d is an equivalent delay time of the control system ($T_d=1.5/f_s$, f_s is the sampling frequency), considering digital execution delay and PWM delay.

In the "dual-loop control" part, if L_{ds} and L_{qs} are different, both i_d^r and i_q^r must be controlled to operate the PMSG at

the maximum torque per ampere (MTPA) operating point. For surface-mounted PMSG, $L_{ds} = L_{qs} = L_s$ and it is relatively easy to control because only i_q^r is controlled and $i_d^r = 0$. In this case, the small-signal model of the control system can be expressed as follows:

$$\text{Voltage loop}: \begin{bmatrix} \tilde{i}_d^{\hat{r}*} \\ \tilde{i}_q^{\hat{r}*} \end{bmatrix} = -\begin{bmatrix} 0 & 0 \\ 0 & K_{vp} + \frac{K_{vi}}{s} \end{bmatrix} (\tilde{v}_{\text{dc}}^* - \tilde{v}_{\text{dc}})$$

$$\tilde{\boldsymbol{i}}_{\boldsymbol{dq}}^{\hat{\boldsymbol{r}}*} = -\boldsymbol{G_{cv}}(\tilde{v}_{\text{dc}}^* - \tilde{v}_{\text{dc}}) \tag{10}$$

$$\text{Current loop}: \begin{bmatrix} \tilde{d}_d^{\hat{r}} \\ \tilde{d}_q^{\hat{r}} \end{bmatrix} = \begin{bmatrix} \frac{2}{V_{\text{dc}}} & 0 \\ 0 & \frac{2}{V_{\text{dc}}} \end{bmatrix} \left(\begin{bmatrix} K_{ipd} + \frac{K_{iid}}{s} & 0 \\ 0 & K_{ipq} + \frac{K_{iiq}}{s} \end{bmatrix} \times \begin{bmatrix} \tilde{i}_d^{\hat{r}*} - \tilde{i}_d^{\hat{r}} \\ \tilde{i}_q^{\hat{r}*} - \tilde{i}_q^{\hat{r}} \end{bmatrix} + \begin{bmatrix} \tilde{e}_d^{\hat{r}} \\ \tilde{e}_q^{\hat{r}} \end{bmatrix} - \begin{bmatrix} \frac{D_d^r}{2} \\ \frac{D_q^r}{2} \end{bmatrix} \tilde{v}_{\text{dc}} \right)$$

$$\tilde{d}_{\boldsymbol{dq}}^{\hat{\boldsymbol{r}}} = \boldsymbol{G_{nor}} \left(\boldsymbol{G_{ci}}(\tilde{\boldsymbol{i}}_{\boldsymbol{dq}}^{\hat{\boldsymbol{r}}*} - \tilde{\boldsymbol{i}}_{\boldsymbol{dq}}^{\hat{\boldsymbol{r}}}) + \tilde{\boldsymbol{e}}_{\boldsymbol{dq}}^{\hat{\boldsymbol{r}}} - \boldsymbol{Y}_{\text{dc}\boldsymbol{v}} \tilde{\boldsymbol{v}}_{\text{dc}} \right). \tag{11}$$

Superscript "$*$" denotes reference value. $\boldsymbol{G_{cv}}$ denotes a transfer function of the dc-link voltage controller, $\boldsymbol{G_{ci}}$ denotes that of the current controller, $\boldsymbol{G_{nor}}$ denotes transformation matrix from voltage to duty factor, $\boldsymbol{Y_{\text{dc}v}}$ links dc-voltage to output voltage, $\tilde{\boldsymbol{e}}_{\boldsymbol{dq}}^{\hat{\boldsymbol{r}}}$ is feedforward component, which can be presented as follows:

$$\begin{bmatrix} \tilde{e}_d^{\hat{r}} \\ \tilde{e}_q^{\hat{r}} \end{bmatrix} = \begin{bmatrix} -\hat{\Omega}_r L_{qs} & 0 \\ 0 & \hat{\Omega}_r L_{ds} \end{bmatrix} \begin{bmatrix} \tilde{i}_d^r \\ \tilde{i}_q^r \end{bmatrix} + \begin{bmatrix} 0 & 0 \\ \frac{\lambda_f s}{-I_q^r + I_d^r} & \frac{\lambda_f s}{-I_q^r + I_d^r} \end{bmatrix} \begin{bmatrix} \tilde{i}_d^r - \tilde{i}_d^{\hat{r}} \\ \tilde{i}_q^r - \tilde{i}_q^{\hat{r}} \end{bmatrix} + \begin{bmatrix} sL_{qs} & 0 \\ 0 & sL_{ds} \end{bmatrix} \begin{bmatrix} \tilde{i}_d^r - \tilde{i}_d^{\hat{r}} \\ \tilde{i}_q^r - \tilde{i}_q^{\hat{r}} \end{bmatrix}$$

$$\tilde{\boldsymbol{e}}_{\boldsymbol{dq}}^{\hat{\boldsymbol{r}}} = \boldsymbol{G_{decI}} \tilde{\boldsymbol{i}}_{\boldsymbol{dq}}^{\hat{\boldsymbol{r}}} + \boldsymbol{G_{emf}} \left(\tilde{\boldsymbol{i}}_{\boldsymbol{dq}}^{\boldsymbol{r}} - \tilde{\boldsymbol{i}}_{\boldsymbol{dq}}^{\hat{\boldsymbol{r}}} \right) + \boldsymbol{G_{decII}} \left(\tilde{\boldsymbol{i}}_{\boldsymbol{dq}}^{\boldsymbol{r}} - \tilde{\boldsymbol{i}}_{\boldsymbol{dq}}^{\hat{\boldsymbol{r}}} \right) \tag{12}$$

where K_{vp} and (K_{ipd}, K_{ipq}) are the proportional gains of dc voltage control and d-q current control, K_{vi} and (K_{iid}, K_{iiq}) are the integral gains of these dual-loop control. These gains can be set as

$$\begin{aligned} K_{vp} &= \frac{2\zeta_{vn}\omega_{vn}C_{dc}V_{dc}}{1.5\Omega_r\lambda_f} \\ K_{vi} &= \frac{\omega_{vn}^2 C_{dc}V_{dc}}{1.5\Omega_r\lambda_f} \\ K_{ipd} &= L_{ds}\omega_c,\ K_{ipq} = L_{qs}\omega_c \\ K_{iid} &= K_{iiq} = R_s\omega_c \end{aligned} \tag{13}$$

where ζ_{vn} and ω_{vn} are the damping factor and the natural frequency of the voltage controller, ω_c is the control bandwidth of the current controller [23]. $\boldsymbol{G_{decI}}$ and $\boldsymbol{G_{decII}}$ denote the gains for current feedforward decoupling, and $\boldsymbol{G_{emf}}$ denotes that of back EMF voltage feedforward decoupling.

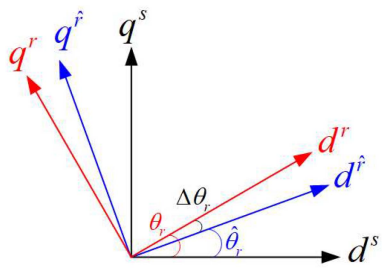

Fig. 5. Rotor reference d-q frame and estimated d-q frame.

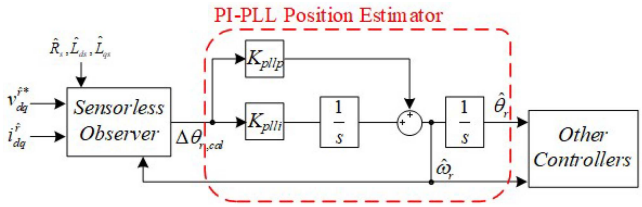

Fig. 6. *PI-PLL* type position estimator of back EMF-based sensorless control.

B. Back EMF-Based Sensorless Control

When the "PMSG+AFE" system estimates the rotor position and speed with the back EMF-based sensorless control, the whole system's small-signal dc impedance and stability are also affected. To analyze the back EMF-based sensorless control, the reference frames are defined as shown in Fig. 5. The superscript "^" denotes variables in the estimated reference d-q frame. When the actual electrical rotor angle is θ_r, and the angle error is $\Delta\theta_r$, the estimated angle $\hat{\theta}_r$ and the estimated speed $\hat{\omega}_r$ can be presented as

$$\begin{aligned} \hat{\theta}_r &= \theta_r - \Delta\theta_r \\ \hat{\omega}_r &= \omega_r - \Delta\omega_r \left(= \frac{d\Delta\theta_r}{dt} \right). \end{aligned} \tag{14}$$

Although several back EMF-based sensorless control ideas have been proposed for angle estimation in the literature, the extended back EMF-based sensorless control is adopted in this article [12]. The extended back EMF-based sensorless control defines the difference between L_{ds} and L_{qs} as L_Δ ($L_\Delta = L_{ds} - L_{qs}$). The sensorless observer gives the estimated angle error from the output voltage, current, and system parameters as

$$\Delta\theta_{r,\text{cal}} = -\frac{e_{ds,est}^{\hat{r}}}{E_{ex,est}} = -\frac{v_d^{\hat{r}*} - (R_s + sL_{ds})i_d^{\hat{r}} + \hat{\omega}_r L_{qs} i_q^{\hat{r}}}{\hat{\omega}_r(L_\Delta i_d^{\hat{r}} + \lambda_f) - sL_\Delta i_q^{\hat{r}}}. \tag{15}$$

$\Delta\theta_{r,\text{cal}}$ is the calculated angle error, and the position estimator gives the estimated rotor angle $\hat{\theta}_r$ and estimated speed $\hat{\omega}_r$ from $\Delta\theta_{r,\text{cal}}$, as shown in Fig. 6. K_{pllp} and K_{plli} are the gains of the position estimator. K_{pllp} and K_{plli} can be set as

$$\begin{aligned} K_{pllp} &= 2\zeta_{plln}\omega_{plln} \\ K_{plli} &= \omega_{plln}^2 \end{aligned} \tag{16}$$

where ζ_{plln} and ω_{plln} are the damping factor and the natural frequency of the position estimator [24]. By making a small angle approximation of trigonometric functions and canceling the steady-state values, the relationship of duty factor between the estimated reference frame and rotor reference frame can be derived as

$$\begin{bmatrix} \tilde{d}_d^{\hat{r}} \\ \tilde{d}_q^{\hat{r}} \end{bmatrix} \approx \begin{bmatrix} \tilde{d}_d^r \\ \tilde{d}_q^r \end{bmatrix} + \begin{bmatrix} D_q^r \tilde{\hat{\theta}}_r \\ -D_d^r \tilde{\hat{\theta}}_r \end{bmatrix}. \tag{17}$$

As previously assumed, although the perturbation of the speed, ω_r is almost negligible thanks to the very slow variation of the engine speed, there is a perturbation in the estimated speed $\hat{\omega}_r$ in the position estimator. From Fig. 6, the integration of estimated speed is estimated angle ($\tilde{\hat{\theta}}_r = \int_0^t \tilde{\hat{\omega}}_r dt$) and relation of $\Delta\tilde{\theta}_r$ and $\tilde{\hat{\theta}}_r$ can be deduced in the Laplace domain as follows:

$$\Delta\tilde{\theta}_r \left(K_{pllp} + \frac{K_{plli}}{s} \right) \frac{1}{s} = \tilde{\hat{\theta}}_r. \tag{18}$$

Applying the small-signal analysis to the duty factor, dc voltage, current, and speed in (15) gives

$$\Delta\tilde{\theta}_r = \left(-\frac{1}{\hat{\Omega}_r L_\Delta I_d^r - L_\Delta s I_q^r + \hat{\Omega}_r \lambda_f} \right) \times \left(\begin{array}{l} \left\{ \frac{V_{dc}}{2} \tilde{d}_d^r - (R_s + L_{ds}s)\tilde{i}_d^r + \hat{\Omega}_r L_{qs} \tilde{i}_q^r \right\} \\ + \left\{ V_q^r - (R_s + L_\Delta s) I_q^r - \hat{\Omega}_r L_{qs} I_d^r \right\} \tilde{\hat{\theta}}_r \end{array} \right). \tag{19}$$

Substituting (19) into (18) gives

$$\tilde{\hat{\theta}}_r = G_{PLL,EMF} \{ \frac{V_{dc}}{2} \tilde{d}_d^r - (R_s + L_{ds}s)\tilde{i}_d^r + \hat{\Omega}_r L_{qs} \tilde{i}_q^r \} \tag{20}$$

with

$$\begin{aligned} G_{PLL,EMF} &= \frac{(sK_{pllp} + K_{plli})}{A_3 s^3 + A_2 s^2 + A_1 s + A_0} \\ A_3 &= -L_\Delta I_q^r \\ A_2 &= \hat{\Omega}_r L_\Delta I_d^r + \hat{\Omega}_r \lambda_f - K_{pllp} L_\Delta I_q^r \\ A_1 &= K_{pllp} V_q^r - K_{pllp} R_s I_q^r \\ &\quad - K_{pllp} \hat{\Omega}_r L_{qs} I_d^r + K_{plli} L_\Delta I_q^r \\ A_0 &= K_{plli}(V_q^r - R_s I_q^r - \hat{\Omega}_r L_{qs} I_d^r). \end{aligned} \tag{21}$$

For surface-mounted PMSG, $L_{ds} = L_{qs} = L_s$ and $L_\Delta = 0$. Then, substituting $L_\Delta = 0$ into (21) gives

$$\begin{aligned} G_{PLL,EMF} &= \frac{(sK_{pllp} + K_{plli})}{A_2 s^2 + A_1 s + A_0} \\ A_2 &= \hat{\Omega}_r \lambda_f \\ A_1 &= K_{pllp} V_q^r - K_{pllp} R_s I_q^r - K_{pllp} \hat{\Omega}_r L_s I_d^r \\ A_0 &= K_{plli}(V_q^r - R_s I_q^r - \hat{\Omega}_r L_s I_d^r). \end{aligned} \tag{22}$$

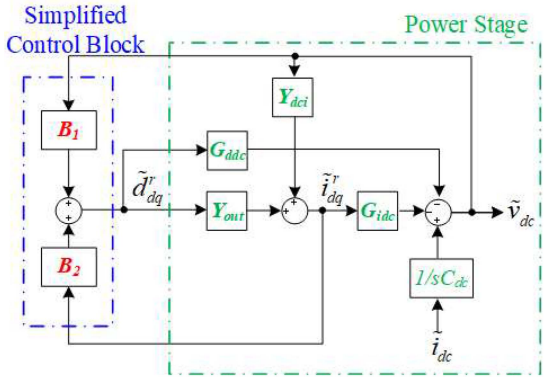

Fig. 7. Simplified small-signal block diagram.

Substituting (20) into (17) gives

$$\begin{bmatrix} \tilde{d}_d^r \\ \tilde{d}_q^r \end{bmatrix} \approx \begin{bmatrix} \tilde{d}_d^{\hat{r}} \\ \tilde{d}_q^{\hat{r}} \end{bmatrix} + \boldsymbol{G_{PLLvv}} \begin{bmatrix} \tilde{d}_d^r \\ \tilde{d}_q^r \end{bmatrix} + \boldsymbol{G_{PLLiv}} \begin{bmatrix} \tilde{i}_d^r \\ \tilde{i}_q^r \end{bmatrix}. \tag{23}$$

Then, $\boldsymbol{G_{PLLvv}}$ and $\boldsymbol{G_{PLLiv}}$ are defined as

$$\begin{aligned} \boldsymbol{G_{PLLvv}} &= G_{PLL,\text{EMF}} \begin{bmatrix} D_q^r \frac{V_{dc}}{2} & 0 \\ -D_d^r \frac{V_{dc}}{2} & 0 \end{bmatrix} \\ \boldsymbol{G_{PLLiv}} &= G_{PLL,\text{EMF}} \begin{bmatrix} -D_q^r (R_s + sL_{ds}) & D_q^r \hat{\Omega}_r L_{qs} \\ D_d^r (R_s + sL_{ds}) & -D_d^r \hat{\Omega}_r L_{qs} \end{bmatrix}. \end{aligned} \tag{24}$$

At the "back EMF-based sensorless control" part in Fig. 4, $\boldsymbol{G_{PLLvv}}$ models the small-signal perturbation path from the duty factor in the exact rotor reference frame to the duty factor in the estimated reference frame. $\boldsymbol{G_{PLLiv}}$ models the small-signal perturbation path from the current in the rotor reference frame to the duty factor in the estimated reference frame. A similar equation can be derived for the current as

$$\begin{bmatrix} \tilde{i}_d^{\hat{r}} \\ \tilde{i}_q^{\hat{r}} \end{bmatrix} = \begin{bmatrix} \tilde{i}_d^r \\ \tilde{i}_q^r \end{bmatrix} + \boldsymbol{G_{PLLii}} \begin{bmatrix} \tilde{i}_d^r \\ \tilde{i}_q^r \end{bmatrix} + \boldsymbol{G_{PLLvi}} \begin{bmatrix} \tilde{d}_d^r \\ \tilde{d}_q^r \end{bmatrix}. \tag{25}$$

Then, $\boldsymbol{G_{PLLii}}$, and $\boldsymbol{G_{PLLvi}}$ are defined as

$$\begin{aligned} \boldsymbol{G_{PLLii}} &= G_{PLL,\text{EMF}} \begin{bmatrix} I_q^r (R_s + sL_{ds}) & -I_q^r \hat{\Omega}_r L_{qs} \\ -I_d^r (R_s + sL_{ds}) & I_d^r \hat{\Omega}_r L_{qs} \end{bmatrix} \\ \boldsymbol{G_{PLLvi}} &= G_{PLL,\text{EMF}} \begin{bmatrix} -I_q^r \frac{V_{dc}}{2} & 0 \\ I_d^r \frac{V_{dc}}{2} & 0 \end{bmatrix}. \end{aligned} \tag{26}$$

At the "back EMF-based sensorless control" part in Fig. 4, $\boldsymbol{G_{PLLii}}$ models the small-signal perturbation path from the rotor reference frame currents to currents in the estimated reference frame. $\boldsymbol{G_{PLLvi}}$ models the small-signal perturbation path from the rotor reference frame duty factor to currents in the estimated reference frame. Based on the small-signal block diagram in Fig. 4, the "dual-loop control" and "back EMF-based sensorless control" parts can be simplified, as shown in Fig. 7 with

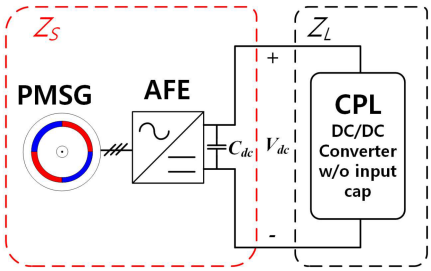

Fig. 8. Source impedance and load impedance.

$$\begin{aligned}\boldsymbol{B_1} &= \{\boldsymbol{G_{del}^{-}}1 - \boldsymbol{G_{pllvv}} - \boldsymbol{G_{nor}}(\boldsymbol{G_{decI}} - \boldsymbol{G_{decII}} \\ &\quad -\boldsymbol{G_{emf}} - \boldsymbol{G_{ci}})\boldsymbol{G_{pllvi}}\}^{-}1 \times \boldsymbol{G_{nor}}\boldsymbol{G_{ci}}\boldsymbol{G_{cv}} - \boldsymbol{Y_{dcv}}\} \\ \boldsymbol{B_2} &= \{\boldsymbol{G_{del}^{-1}} - \boldsymbol{G_{pllvv}} - \boldsymbol{G_{nor}}(\boldsymbol{G_{decI}} - \boldsymbol{G_{decII}} \\ &\quad - \boldsymbol{G_{emf}} - \boldsymbol{G_{ci}})\boldsymbol{G_{pllvi}}\}^{-1} \times \{\boldsymbol{G_{nor}}(\boldsymbol{G_{decI}} \\ &\quad - \boldsymbol{G_{decII}} - \boldsymbol{G_{emf}} - \boldsymbol{G_{ci}})(\boldsymbol{I}+\boldsymbol{G_{pllii}}) \\ &\quad + \boldsymbol{G_{plliv}} + \boldsymbol{G_{nor}}(\boldsymbol{G_{decII}} + \boldsymbol{G_{emf}})\}. \end{aligned} \tag{27}$$

Then, the dc impedance model of "PMSG+AFE" system can be expressed as

$$\begin{aligned} Z_S &= \tilde{v}_{\rm dc}(\tilde{i}_{\rm dc})^{-1} = \frac{\tilde{v}_{\rm dc}}{\tilde{i}_{\rm dc}} \\ &= \frac{1/sC_{\rm dc}}{1+\boldsymbol{G_{ddc}}\boldsymbol{B_1}+(\boldsymbol{G_{ddc}}\boldsymbol{B_2}+\boldsymbol{G_{idc}})(\boldsymbol{I}-\boldsymbol{Y_{out}}\boldsymbol{B_2})^{-1}(\boldsymbol{Y_{out}}\boldsymbol{B_1}+\boldsymbol{Y_{dci}})}. \end{aligned} \tag{28}$$

III. Stability Analysis Using the Proposed Model

This section analyzes the stability of the "PMSG+AFE" system using the proposed model. First, the effect of dual-loop control on the system stability is analyzed. Second, the effect of sensorless control on the system stability is analyzed. Finally, the system stability is analyzed when the estimated inductance parameter is different from the actual parameter. The stator impedance of surface-mounted PMSG is set to about 60% [25], and the current control bandwidth is set to 200 Hz in consideration of the MW-class PMSG. All system parameters are listed in Table I. Fig. 8 shows the concept of the source impedance Z_S and load impedance Z_L. CPL is implemented with a current control bandwidth of 500 Hz. The impedance of the CPL, Z_L is calculated as follows [19]:

$$Z_L = -\frac{V_{\rm dc}^2}{P_{\rm load}^*} \tag{29}$$

where $P_{\rm load}^*$ is a reference of CPL.

A. Effect of the Dual-Loop Control on the System Stability

Fig. 9 shows the effect of the dual-loop control on the stability of the system. First, Fig. 9(a) shows the system stability according to the control bandwidth of the current control loop when the natural frequency of the dc voltage control loop, ω_{vn}, is 45 Hz.

TABLE I
Parameters of "PMSG+AFE" System

Parameter	Value
Load power P_{load}	6000 W
Flux linkage of the permanent magnet λ_f	0.164 Wb
Stator inductance L_s (L_s=L_{ds}=L_{qs})	1.9 mH
Stator resistance R_s	0.05 Ω
Number of pole pairs p	4
Mechanical rotating speed Ω_m	1200 r/min
Fundamental frequency Ω_r	80 x 2π rad/s
d-axis current I_d^r	0 A
q-axis current I_q^r	-51 A
DC voltage V_{dc}	250 V
DC-link capacitor C_{dc}	425 μF
Switching frequency f_{sw}	10 kHz
Current controller bandwidth ω_c	200 x 2π rad/s
Voltage controller natural frequency ω_{vn}	45 x 2π rad/s
Voltage controller damping factor ξ_{vn}	1
Sensorless control natural frequency ω_{plln}	30 x 2π rad/s
Sensorless control damping factor ξ_{plln}	0.707
Control delay T_d	150 μs

The current control loop is a lower-level control of the dual-loop control. The larger the control bandwidth of the current control loop, the more stable the system becomes. However, since the control bandwidth of the current control loop is limited by the sampling frequency of the AFE, it is essential to set the control bandwidth suitable for the system considering the sampling frequency. Next, Fig. 9(b) shows the system stability according to the natural frequency of the dc voltage control loop when the control bandwidth of the current control loop, ω_{cc}, is 200 Hz. DC voltage control loop is a higher-level control of the dual-loop control. In the case of a dc voltage control loop, it can be seen that the proper natural frequency can be selected according to the control bandwidth of the current control. Therefore, system stability analysis using dc impedance and Nyquist criterion is essential for the dual-loop control system design and gain setting.

B. Effect of the Sensorless Control on the System Stability

Fig. 10 shows the effect of the sensorless control on the stability of the system. When the natural frequency of the sensorless control ω_{plln} is 0 Hz, sensorless is not applied, and when it is not 0 Hz, sensorless is applied. When ω_{plln} is 0 Hz, it is most stable, and as ω_{plln} is higher, it becomes less stable, but it is not unstable in the range of 0–50 Hz. It can be seen that ω_{plln} of the sensorless control has little effect on the system stability. As shown in Fig. 6, the sensorless observer estimates the angular error using the parameters of PMSG and state variables (voltage, current,

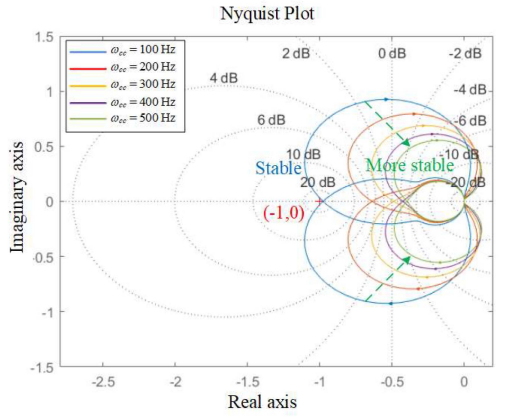

(a)

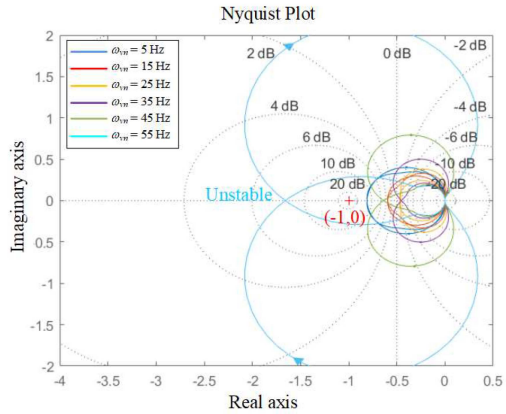

(b)

Fig. 9. Nyquist plots. (a) Effect of the current control loop. (b) Effect of the dc voltage control loop.

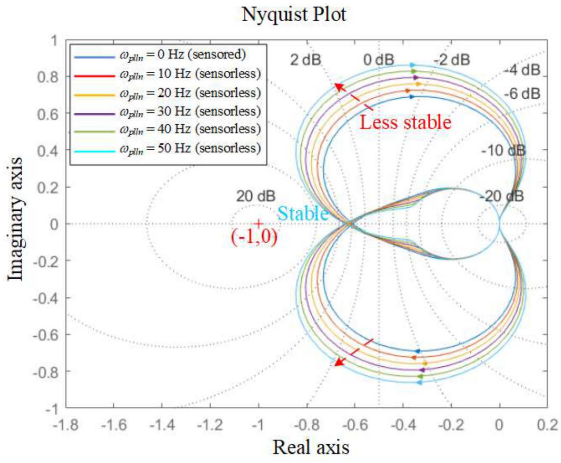

Fig. 10. Nyquist plot: effect of the sensorless control.

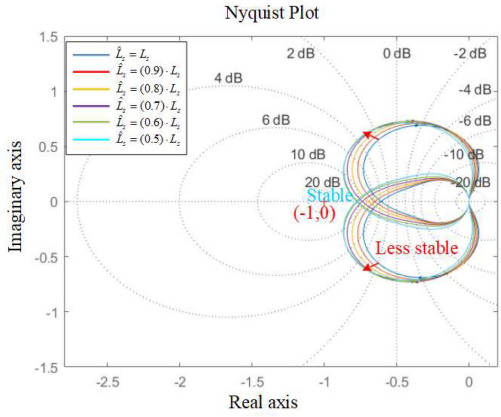

(a)

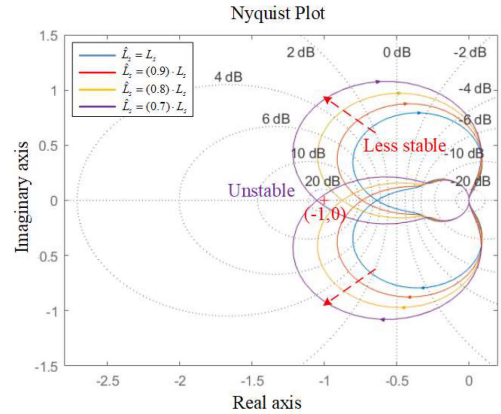

(b)

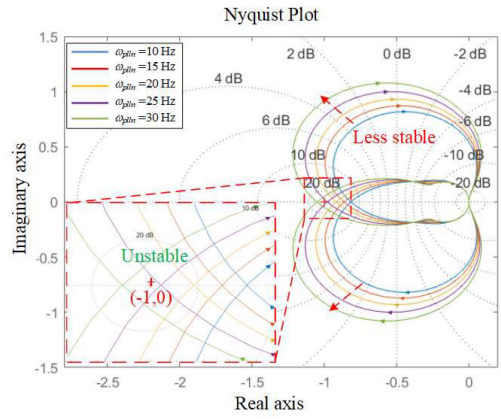

(c)

Fig. 11. Nyquist plots. (a) Position sensored control. (b) Sensorless control. (c) Sensorless control with $\hat{L}_s = (0.7)L_s$.

speed). Therefore, the sensorless control does not significantly affect the system stability under the exact parameter condition.

C. Effect of the Parameter Error on the System Stability

Fig. 11 shows the effect of the parameter error on the stability of the system. Among the various kinds of parameter errors, error in the estimated inductance value, $\hat{L}_s$ is the most influential for many controllers as it is applied to the current forward decoupling (12), the proportional gain of the current controller (13), and the sensorless observer (15). Fig. 11(a) shows the stability analysis result when the error of the estimated inductance value $\hat{L}_s$ affects only the current control loop. Since the position sensor control is applied, the error of the estimated inductance value $\hat{L}_s$ does not affect the sensorless control. Even if the estimated inductance value $\hat{L}_s$ differs from the actual value

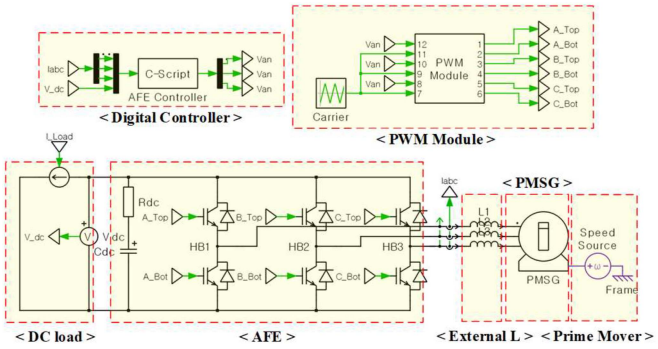

Fig. 12. Simulation model: 6 kW "PMSG+AFE" system and dc load.

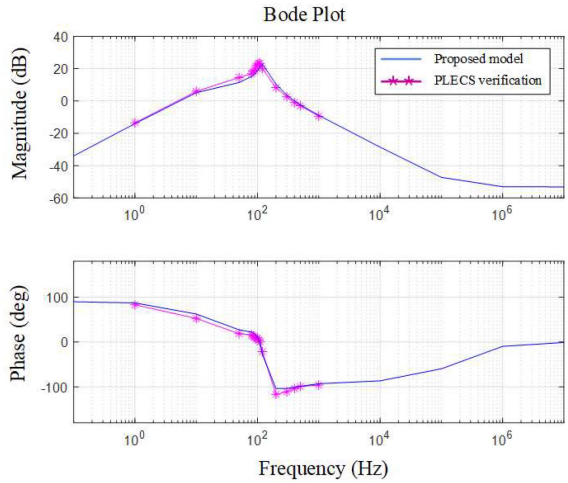

Fig. 13. Proposed model and PLECS verification.

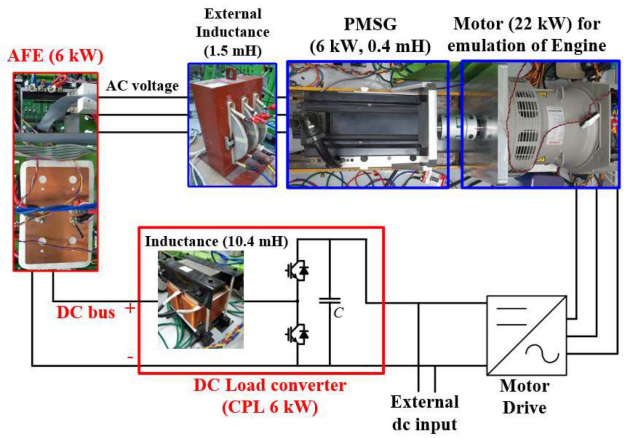

Fig. 14. Experimental setup: 6-kW "PMSG+AFE" system and a dc/dc converter for CPL.

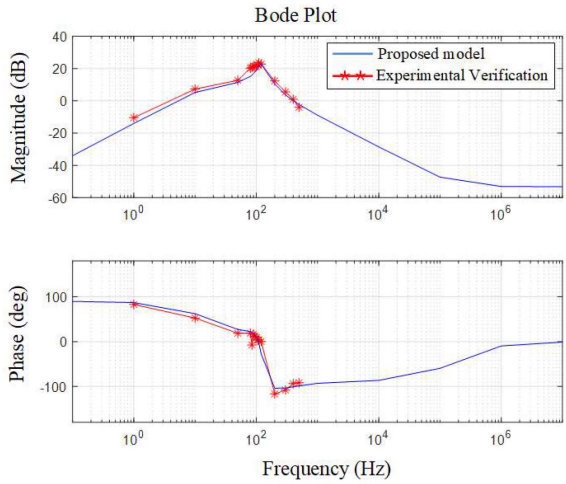

Fig. 15. Proposed model and experimental verification.

by 50%, it does not significantly affect the stability. Therefore, the error of the estimated inductance value $\hat{L}_s$ has little effect on the system stability in the position-sensored control. Fig. 11(b) shows the stability analysis result when the error of the estimated inductance value $\hat{L}_s$ affects both the current control loop and the position sensorless control. It becomes unstable if the estimated inductance value $\hat{L}_s$ differs from the actual value by 30%. Fig. 11(c) shows the effect of position sensorless control when the estimated inductance value $\hat{L}_s$ differs from the actual value by 30%. Comparing Figs. 11(c) and 10 show the effect of position sensorless control on the system stability when the estimated inductance value $\hat{L}_s$ differs from the actual value and when there is no difference. Therefore, if the estimated inductance value of the PMSG varies significantly depending on the operating condition or the estimated inductance value is uncertain, "PMSG+AFE" system can be unstable with dual-loop control and position sensorless control.

IV. Simulation and Experimental Results

A. Simulation Setup and Verification of the Impedance Z_S

To verify the proposed dc impedance Z_S (28) and stability analysis, computer simulations are conducted using a power electronics simulation language, PLECS, as shown in Fig. 12. Prime mover is modeled as the ideal rotational speed source. The parameters of PMSG were set as listed in Table I. AFE consists of ideal switches and is controlled by a digital controller, which is the same as the experimental C-programing code. Current control, dc voltage control, and sensorless control are implemented in the digital controller. The PWM module block implements the PWM operation of the switches in the AFE. The dc load is an ideal current source containing dc and ac sinusoidal current. The source impedance Z_S can be measured by applying the ideal current source and observing the dc voltage fluctuation of the AFE. Verification using PLECS simulation was performed up to 1 kHz. The reason is that there is interference with the switching frequency of 10 kHz, and the measurement is inaccurate above 1 kHz. Fig. 13 shows the proposed model and PLECS verification at the natural frequency of sensorless control ω_{plln} is 30 Hz, and the estimated inductance value $\hat{L}_s$ differs from the actual value by 30%. The proposed model is consistent with the simulation measurement. Therefore, it can be said that the proposed impedance model reflecting the effects

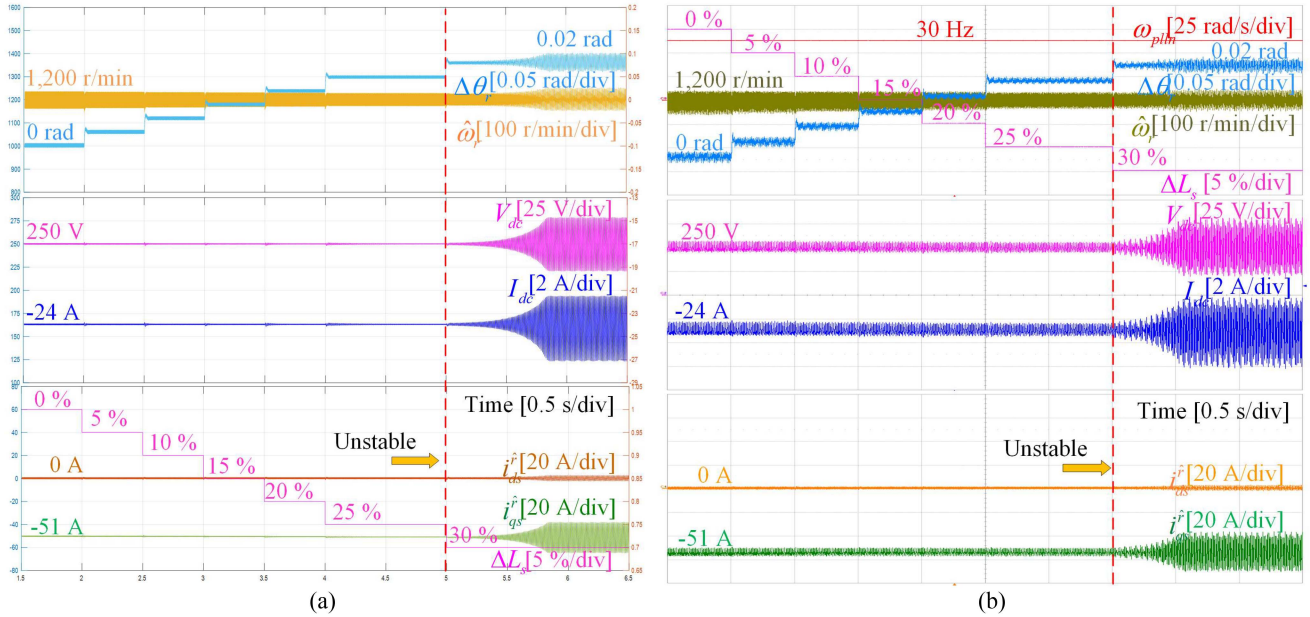

Fig. 16. Verification of the stability analysis in Fig. 11(b). (a) Simulation. (b) Experiment.

of the current control, voltage control, and sensorless control has been verified by the computer simulation.

B. *Experimental Setup and Verification of the Impedance* Z_S

A small-scale experimental setup is organized to verify the proposed dc impedance Z_S (28), as shown in Fig. 14. The corresponding parameters are listed in Table I. Considering the generator's parameter, the rated dc voltage was set to 250 V, and the mechanical rotating speed was set to 1200 r/min. As a prime mover, a wounded rotor synchronous motor of 22 kW, 440 V, and 60 Hz is utilized to emulate the characteristics of the diesel engine. As a generator, 6 kW, 1200 r/min surface-mounted PMSG is adopted. Since the per-unit stator inductance of the small PMSG is much smaller than that of the MW-class PMSG in general, the external inductance of 1.5 mH is inserted between PMSG and AFE to emulate large PMSG. Then, the total per-unit inductance of PMSG is set to 60%, similar to the d-axis inductance of MW-class PMSG [24]. The AFE is a typical two-level three-phase inverter and adopted 600 V, 150 A, IGBT. The dual-loop control and back EMF-based sensorless control are realized through TMS320F28377 DSP control board, and the signal sampling frequency is set as 10 kHz. The dc-link capacitor bank is 425 μF. The dc output side of the AFE is connected to the dc bus, and a typical bi-directional dc/dc converter is adopted as the dc load. The inductance side of the dc/dc converter is connected to the dc bus because dc capacitance on both sides complicates the system stability analysis. Therefore, to simplify the system, there is only inductance on the load side. In this configuration, the capacitor at the output stage of the dc/dc converter does not affect the load impedance. In addition, the inductance instantaneously acts as a current source and is easy to control to operate as a CPL. The current control bandwidth of the dc/dc converter is set to 500 Hz, which is high enough to operate as a CPL. The output power of the dc/dc converter is regenerated by the input of the motor drive that runs the 22 kW motor for engine emulation.

The source impedance Z_S is measured by applying the sum of the steady-state dc and disturbance ac to the dc output of the AFE. The steady-state dc is -24 A, and the disturbance ac is 0.1–0.5 A, 1–500 Hz. The source impedance Z_S can be calculated from the amount of fluctuation in the dc output voltage of AFE. Since AFE and dc/dc converter are power electronics devices, various harmonics including switching components appear in the dc voltage waveform, so it is difficult to identify them visually. Therefore, it is possible to measure the voltage fluctuation to the frequency of the applied disturbance current by using the FFT function of the oscilloscope. If the fluctuation of the dc voltage due to the disturbance current is too large, it may cause instability in the system. Therefore, the amplitude of the disturbance current was adjusted so that the dc voltage fluctuation does not exceed ± 10 V. If the sinusoidal frequency is close to the switching frequency of 10 kHz, the interference makes the measurement inaccurate. The maximum value that determines stability and instability occurs below 200 Hz, and verification up to 500 Hz would be sufficient. Fig. 15 shows the proposed model and experimental verification at the natural frequency of sensorless control ω_{plln} is 30 Hz, and the estimated inductance value $\hat{L}_s$ differs from the actual value by 30%. The maximum value of the source impedance Z_S is slightly larger in the experimental verification and occurred at 100 Hz on the proposed model and 85 Hz on the experimental verification. Since the shape of the waveform between 80 and 110 Hz is important, many measurement points are placed in this area. The overall shape of the waveform is similar to that of the waveform from the proposed model and that from experimental verification. Therefore, it can be noted that the proposed dc impedance Z_S (28) is verified by experiments.

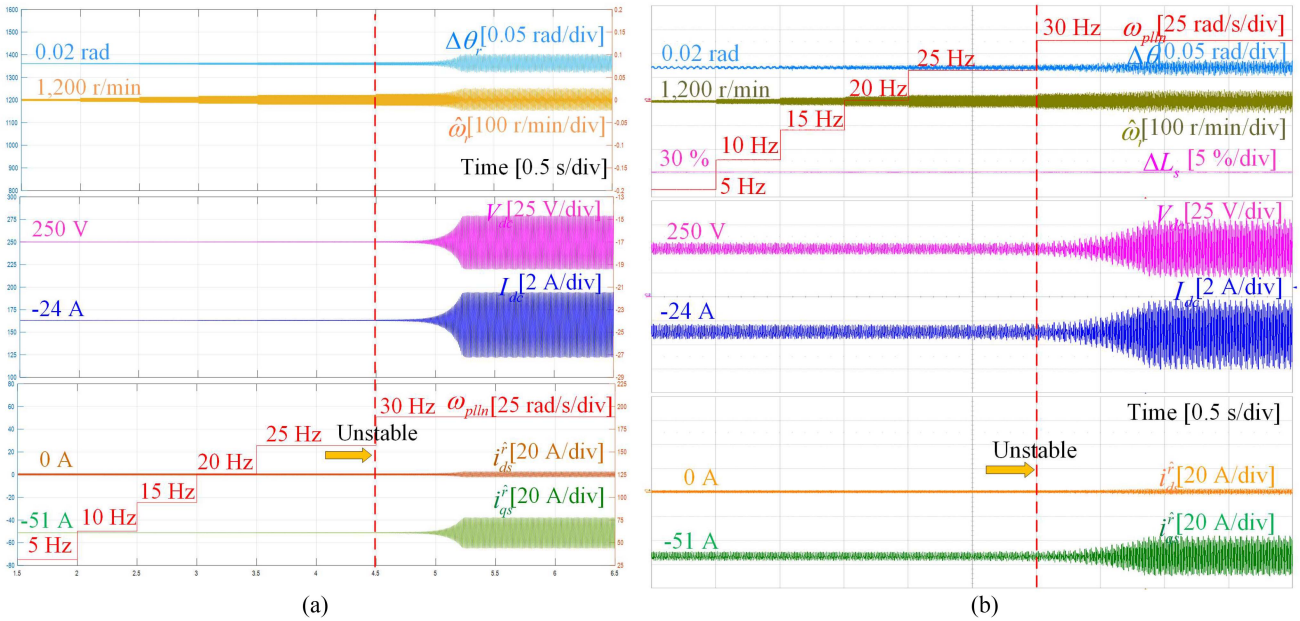

Fig. 17. Verification of the stability analysis in Fig. 11(c). (a) Simulation. (b) Experiment.

C. Simulation and Experimental Results

To verify the stability analysis in Fig. 11(b), PLECS simulations and experiments were performed with the ideal PMSG model and actual small-scale experimental PMSG setup. Fig. 16(a) shows the PLECS simulation result and Fig. 16(b) shows the experimental result. In Fig. 16, the cyan and yellow line in the figure depict $\Delta\theta_r$ and $\hat{\omega}_r$, respectively. The magenta and blue line in the figure are $V_{\rm dc}$ and $I_{\rm dc}$, respectively. The orange, green, and magenta lines in the figure are $i_d^{\hat{r}}$, $i_q^{\hat{r}}$, and $\Delta L_s = (L_s - \hat{L}_s)/L_s$, respectively. The sensorless control loses its stability when the estimated inductance value $\hat{L}_s$ differs from the actual value by 30%. This is consistent with the stability analysis in Fig. 11(b). The experimental result of Fig. 16(b) is the same as the simulation result of Fig. 16(a). In both the experimental and simulation results, the estimated inductance value $\hat{L}_s$ decreases by 5% every 0.5 s. In the first 0.5 s, there is no error in the estimated inductance value $\hat{L}_s$, and the sensorless control accurately estimates the position of the rotor, so the angular error $\Delta\theta_r$ is also 0 rad. However, as the error of the estimated inductance value $\hat{L}_s$ increases, angular error $\Delta\theta_r$ gradually increases. The error in the increased estimated inductance value $\hat{L}_s$ weakens the proportional gain of the current controller (13) and forward decoupling (12). It affects the performance of the sensorless observer (15). Eventually, it makes the system unstable.

Verification of the stability analysis in Fig. 11(c) is also shown in Fig. 17(a) and (b). In this case, the natural frequency of sensorless control ω_{plln} increases when the estimated inductance $\hat{L}_s$ differs from the actual value by 30%. As shown in Fig. 17(a) and (b), the sensorless control loses its stability when the natural frequency of sensorless control ω_{plln} becomes 30 Hz. It can be said that the stability analysis through Nyquist plots in Fig. 11(b) and (c) well match the simulation and experiment results in Figs. 16 and 17.

These simulation and experimental results show that the proposed impedance model and stability analysis is feasible in an actual "PMSG+AFE" system with dual-loop control and back EMF-based sensorless control.

V. Conclusion

This article proposed and verified the impedance model of the "PMSG+AFE" system with dual-loop and back EMF-based sensorless control for a dc grid marine vessel. If the parameters of the PMSG were accurate enough, there was little effect on the stability according to the bandwidth of the sensorless control. However, if there were an error in the estimated inductance parameter, the high bandwidth of the sensorless control would deteriorate the system's stability. The proposed model and stability analysis were verified through PLECS simulation and experiments. The proposed model is consistent with the simulation measurement and experimental measurement. The stability analysis is also consistent with the PLECS simulation and experiment. With the proposed impedance model, the stability analysis of systems with other complex control strategies can be carried out. For the dc marine vessels with sensorless control, the system can be designed and optimized by considering the proposed model.

References

[1] F. Gao and S. Bozhko, "Modeling and impedance analysis of a single DC bus-based multiple-source multiple-load electrical power system," *IEEE Trans. Transp. Electrific.*, vol. 2, no. 3, pp. 335–346, Sep. 2016, doi: 10.1109/TTE.2016.2592680.

[2] G. Sulligoi, A. Tessarolo, V. Benucci, A. M. Trapani, M. Baret, and F. Luise, "Shipboard power generation: Design and development of a medium-voltage DC generation system," *IEEE Ind. Appl. Mag.*, vol. 19, no. 4, pp. 47–55, Jul./Aug. 2013.
[3] D. Dujic and U. Javaid, "MVDC power distribution networks and technologies for marine applications," in *Proc. ECPE Workshop*, 2018, pp. 1–28.
[4] S. O. Settemsdal, "DC power grids-SOGO bluedrive plusc-enhanced safety in power plant solutions proven by testing," in *Proc. ECPE Workshop, DC Grids, Technol. Appl.*, 2018, pp. 1–19.
[5] S.-Y. Kim, B.-G. Cho, and S.-K. Sul, "Consideration of active-front-end rectifier for electric propulsion navy ship," in *Proc. IEEE Energy Convers. Congr. Expo.*, 2013, pp. 13–19.
[6] Y.-K. Son, S.-Y. Lee, and S.-K. Sul, "DC power system for fishing boat," in *Proc. IEEE Int. Conf. Power Electron., Drives Energy Syst.*, 2018, pp. 1–6, doi: 10.1109/PEDES.2018.8707631.
[7] Z.-X. Xiao et al., "Operation control for improving energy efficiency of shipboard microgrid including bow thrusters and hybrid energy storages," *IEEE Trans. Transp. Electrific.*, vol. 6, no. 2, pp. 856–868, Jun. 2020, doi: 10.1109/TTE.2020.2992735.
[8] G. Sulligoi, A. Vicenzutti, and R. Menis, "All-electric ship design: From electrical propulsion to integrated electrical and electronic power systems," *IEEE Trans. Transp. Electrific.*, vol. 2, no. 4, pp. 507–521, Dec. 2016, doi: 10.1109/TTE.2016.2598078.
[9] "Drives for every demand-the SINAMICS family of medium voltage drives," SIEMENS, Munich, Germany, 2019. [Online]. Available: https://assets.new.siemens.com/siemens/assets/api/uuid:dc24aadc-96b8-40aa-98f9-12c53fbbb774/poster-sinamics-mv-drives-en.pdf
[10] INGEDRIVE LV200, INGETEAM, 2021. [Online]. Available: https://www.ingeteam.com/Portals/0/Catalogo/Producto/Documento/PRD_4308_Archivo_ingedrive-lv200-tf01ipt-mi01-.pdf
[11] INGEDRIVE LV900, INGETEAM, 2021. [Online]. Available: https://www.ingeteam.com/Portals/0/Catalogo/Sector/Documento/SSE_4254_Archivo_pc00ipt-mi00-catalogo-mv900.pdf
[12] G. Wang, M. Valla, and J. Solsona, "Position sensorless permanent magnet synchronous machine drives—A review," *IEEE Trans. Ind. Electron.*, vol. 67, no. 7, pp. 5830–5842, Jul. 2020, doi: 10.1109/TIE.2019.2955409.
[13] S. D. Sudhoff, K. A. Corzine, S. F. Glover, H. J. Hegner, and H. N. Robey, "DC link stabilized field oriented control of electric propulsion systems," *IEEE Trans. Energy Convers.*, vol. 13, no. 1, pp. 27–33, Mar. 1998, doi: 10.1109/60.658200.
[14] C. M. Wildrick, F. C. Lee, B. H. Cho, and B. Choi, "A method of defining the load impedance specification for a stable distributed power system," *IEEE Trans. Power Electron.*, vol. 10, no. 3, pp. 280–285, May 1995, doi: 10.1109/63.387992.
[15] S. D. Sudhoff, S. F. Glover, P. T. Lamm, D. H. Schmucker, and D. E. Delisle, "Admittance space stability analysis of power electronic systems," *IEEE Trans. Aerosp. Electron. Syst.*, vol. 36, no. 3, pp. 965–973, Jul. 2000, doi: 10.1109/7.869516.
[16] D. Xue, J. Liu, Z. Liu, Y. Tu, and T. Liu, "Modeling and analysis of DC terminal impedance of voltage-source converters with different control modes," *IEEE Trans. Power Electron.*, vol. 35, no. 6, pp. 5883–5896, Jun. 2020, doi: 10.1109/TPEL.2019.2953118.
[17] H. Nian, J. Yang, B. Hu, Y. Jiao, Y. Xu, and M. Li, "Stability analysis and impedance reshaping method for DC resonance in VSCs-based power system," *IEEE Trans. Energy Convers.*, vol. 36, no. 4, pp. 3344–3354, Dec. 2021, doi: 10.1109/TEC.2021.3066201.
[18] J. Huang, Z. Zhang, and J. Han, "Stability analysis of permanent magnet generator system with load current compensating method," *IEEE Trans. Smart Grid*, vol. 13, no. 1, pp. 58–70, Jan. 2022, doi: 10.1109/TSG.2021.3112707.
[19] J. Yang et al., "Modeling and stability enhancement of a permanent magnet synchronous gen erator based DC system for more electric aircraft," *IEEE Trans. Ind. Electron.*, vol. 69, no. 3, pp. 2511–2520, Mar. 2022, doi: 10.1109/TIE.2021.3066934.
[20] X. Lang et al., "Stability improvement of onboard HVdc grid and engine using an advanced power generation center for the more-electric aircraft," *IEEE Trans. Transp. Electrific.*, vol. 8, no. 1, pp. 660–674, Mar. 2022, doi: 10.1109/TTE.2021.3095256.
[21] Wärtsilä 46DF PRODUCT GUIDE. Wärtsilä, Helsinki, Finland, 2019. [Online]. Available: https://www.wartsila.com/docs/default-source/product-files/engines/df-engine/product-guide-o-e-w46df.pdf?utm_source=engines&utm_medium=dfengines&utm_term=w46df&utm_content=productguide&utm_campaign=msleadscoring
[22] Y. Li, Z. Shuai, X. Liu, Y. Hong, X. Wu, and Z. J. Shen, "Stability investigation of bidirectional AC-DC converter considering operating conditions," *IEEE Access*, vol. 8, pp. 131499–131510, 2020, doi: 10.1109/ACCESS.2020.3009360.
[23] S.-K. Sul, *Control of Electric Machine Drive Systems*. Hoboken, NJ, USA: Wiley, 2010.
[24] J. Yoo and S.-K. Sul, "Stability analysis of PI-controller-type position estimator for sensorless PMSM drives in flux weakening region," in *Proc. IEEE Transp. Electrific. Conf.*, 2021, pp. 434–438, doi: 10.1109/ITEC51675.2021.9490071.
[25] Y.-K. Son, S.-Y. Lee, S. Ko, Y.-W. Kim, and S.-K. Sul, "Maritime DC power system with generation topology consisting of combination of permanent magnet generator and diode rectifier," *IEEE Trans. Transp. Electrific.*, vol. 6, no. 2, pp. 869–880, Jun. 2020, doi: 10.1109/TTE.2020.2992474.

Young-Wook Kim (Graduate Student Member, IEEE) was born in South Korea, in 1983. He received the B.S. and M.S. degrees in electrical engineering, in 2006 and 2008, respectively, from the Seoul National University, Seoul, South Korea, where he is currently working toward the Ph.D. degree in electrical engineering.

From 2008 to 2018, he was a senior researcher with Hyosung Heavy Industry Company, Seoul, South Korea. His current research interests include power electronics, design and control of electric machine, and shipboard electric power system.

Seung-Ki Sul (Fellow, IEEE) received the B.S., M.S., and Ph.D. degrees in electrical engineering from the Seoul National University, Seoul, South Korea, in 1980, 1983, and 1986, respectively.

From 1986 to 1988, he was an Associate Researcher with the Department of Electrical and Computer Engineering, University of Wisconsin, Madison, WI, USA. From 1988 to 1990, he was a Principal Research Engineer with LG Industrial Systems Company, Anyang, South Korea. Since 1991, he has been a member of faculty with the School of the Electrical and Computer Engineering, Seoul National University, where he is currently a Professor. He has authored or coauthored more than 150 IEEE journal papers and a total of more than 340 international conference papers in the area of power electronics. For the last 40 years of R&D experience, he involved in over 150 industry-sponsored collaboration projects in the area of elevator drive, steel mill plant, home appliance, PCS of renewables, electric/hybrid vehicles, and ship propulsion. His current research interests include position sensorless control of electrical machines, electric/hybrid vehicles and ship drives, and power-converter circuits based on SiC MOSFET.

Dr. Sul was the Program Chair of IEEE Power Electronics Specialists Conference in 2006 and the General Chair of IEEE International Conference on Power Electronics and ECCE-Asia in 2011. From 2011 to 2014, he was the Editor-in-Chief for the *Journal of Power Electronics*, which is an SCIE-registered journal, published by the Korean Institute of Power Electronics (KIPE), Seoul, South Korea. For year 2015, he was the President of KIPE. He was the recipient of the 2015 IEEE Transaction 1st and 2nd Paper Awards on Industrial Application, simultaneously, 2016 Outstanding Achievement Award of the IEEE Industrial Application Society, and 2017 Newell award sponsored IEEE Power Electronics Society.